Journal of Materials Research and Technology 41 (2026) 1630–1643

Contents lists available at ScienceDirect

Journal of Materials Research and Technology

journal homepage: www.elsevier.com/locate/jmrt

Improvement of microstructure and mechanical property of Al–2Fe alloy though an in-situ reaction of Fe_2O_3 powder in Al–Mg melts

Hao Lian [a], Z.M. Shi [a,*], Wenlong Yu [a], Y. Wang [b], Wenbin Wang [a], Na Pang [a]

[a] School of Materials Science and Engineering, Inner Mongolia University of Technology, Hohhot, 010051, China
[b] Institute of Materials and Manufacturing, Brunel University London, UB83PH, UK

ARTICLE INFO

Keywords:
Al–Fe
Composite
In-situ reaction
$MgAl_2O_4$
Refinement
Reinforcement
Microstructure
Mechanical property

ABSTRACT

Al–Fe based alloys exhibit excellent high heat-resistance property but suffer from low strength and hardness because the soft aluminum matrix is interrupted by coarse needle/flake-like Al_3Fe phases. To refine Al_3Fe phases and strengthen Al matrix, we developed an in-situ liquid-solid reaction strategy based on Al–Mg–Fe_2O_3 system to fabricate a $MgAl_2O_4$ particle-reinforced Al–2Fe composite. Results show that the formation of $MgAl_2O_4$ particles is primarily governed by the diffusion of Mg, Al, and O elements and the substitution of Mg and Al for Fe in Fe_2O_3. $MgAl_2O_4$ particles with nano and submicron sizes are uniformly dispersed in Al matrix. Those in-situ formed nano and submicron particles serve as heterogeneous nucleation sites of Al_3Fe crystals by providing coherent interfaces; while only the nanosized $MgAl_2O_4$ particles acted as nucleation sites of Al crystals. Compared with the Al–2Fe alloy, the sizes of Al grains and Al_3Fe phases in composite were reduced by 54.7 % and 34.5 %, respectively, accompanied by increases of 36.9 %, 47.7 %, and 40.5 % in yield strength, ultimate tensile strength, and Vickers hardness. Furthermore, the elongation was slightly decreased from 16.5 % to 13.0 %. The improvement of mechanical properties are attributed to the in-situ-formed $MgAl_2O_4$ particles, which refine the Al grains and Al_3Fe phase and strengthen the Al matrix.

1. Introduction

Al–Fe alloys are used to fabricate assemblies subjecting to heat, corrosion, and wear. In this case, high strength, hardness, and plasticity are essential for the plastic processing and applicability of products. However, the mechanical properties of Al–Fe alloys are severely worsened owing to the coarse needle/flake-like Al_3Fe phases separating Al matrix [1,2]. The key to improving the properties lies in refining the microstructure and strengthening of Al matrix, in which melts modification is an effective strategy.

The introduction of refiners such as Al–Ti–B, Al–Ti–C and TiB_2 [3,4], as well as modifiers of rare earth [5,6] and other alloying elements [7,8] can facilitate nucleation of α-Al and Al_3Fe crystals or resist their growth in solidification, thereby enhancing the plasticity. However, these approaches exert only a limited influence on strength and hardness; although increasing the addition of alloying elements can improve strength and hardness, it largely reduces the plasticity. Additionally, speed-up of cooling rate [9], semisolid casting [10], and squeezing casting [11] can also refine the microstructure by strengthening crystallization, however, these methods are difficult to be used for fabrication of large-bulk ingots.

Despite those limitations in improving the mechanical properties of Al–Fe based alloys, the development of particle-reinforced composites has emerged as an effective strategy, with reinforcements including Al_2O_3, AlN, TiB_2, TiC, and ZrB_2 [12]. Notably, uniformly distributed fine particles with coherent relationships to Al crystals have minimal adverse influence on plasticity; however, the larger particles located at grain boundaries show only secondary strengthening effect, and significantly reduce plasticity. This indicates that formation of the fine particles is crucial for preparation of high-quality Al based composites [13–15].

Many pioneer works have confirmed the feasibility of fine particles inducing mechanical reinforcement. Li et al. [16] fabricated nanosized SiC particle-reinforced Al-based composites; they found that when the volume fraction of SiC particles reached to 7 vol%, the average grain size of α-Al was refined from 270 μm to 90 μm, the yield strength and tensile strength were increased by 172 % and 156 %, respectively, while the elongation was greatly decreased from 40 % to 28 %. Su et al. [17] incorporated nanosized Al_2O_3 particles into AA2024 aluminum alloys; when the mass fraction of Al_2O_3 particles reached to 2 wt%, the yield strength and tensile strength were increased by 37 % and 81 %,

* Corresponding author.
E-mail address: shizm@imut.edu.cn (Z.M. Shi).

https://doi.org/10.1016/j.jmrt.2026.01.072
Received 10 November 2025; Received in revised form 27 December 2025; Accepted 9 January 2026
Available online 14 January 2026

respectively, the elongation was reduced to only 0.5 %. Arun et al. [18] synthesized the B_4C nanoparticle reinforced AA8011 alloy by a high-energy stirring casting; addition of the nanosized B_4C had significant improvements on hardness, strength, and fatigue life but resulted in a transition of fracture mode from ductile to brittle. 1.5 wt% B_4C addition made the yield strength, ultimate strength, and hardness increase from 33.3 MPa, 107.0 MPa, and 36.0 HV to 61.7 MPa, 123.0 MPa, and 49.7 HV respectively, but the elongation was reduced from 26.4 % to 18.2 %.

Importantly, it was noticed that these researches mainly adopted ex-situ particle reinforcements, which may have weaker combination with Al matrix because the particle surfaces are prone to contamination prior to processing. These particles are difficult to form coherent relationships with Al matrix to refine the microstructure and therefore greatly decrease the plastic properties of alloys.

To overcome the limitations of ex-situ reinforcements, in-situ liquid–solid and solid–solid reactions provide an effective route to fabricate particle-reinforced Al-based composites, since the in-situ formed particles avoid surface contamination and exhibit strong interfacial bonding with the Al matrix [19,20].

The in-situ-generated spinel ($MgAl_2O_4$) particles is regarded as the most effective grain-refiner and reinforcement in Al-Based alloys [21,22] because of (i) its outstanding heterologous nucleation ability, (ii) better wettability to Al melts, (iii) good compatibility to Al matrix (α-Al) [23], which effectively reduces interfacial energy and significantly increases the nucleation rate during solidification. Moreover, spinel is thermodynamically stable and cannot be dissolved or decomposed in the melts, thereby avoiding refinement recession [24].

Many kinds of oxides such as ZnO, SiO_2, CuO, and B_2O_3 can be used as the oxygen source; however, Mg addition is essential for formation of $MgAl_2O_4$ reinforcement in each system. Jia et al. [25] prepared an in-situ formed $MgAl_2O_4$ particle-reinforced Al–Zn–Mg composite based on the Al–Mg–ZnO system using reactive sintering combined with ball milling. The results showed that the submicron $MgAl_2O_4$ particles formed within the composite significantly refined the Al grain size from 2.47 μm to 1.39 μm. The yield strength and tensile strength reached 347.0 MPa and 505.0 MPa, respectively, representing increases of 27.1 % and 28.8 % compared to the matrix alloy. Crystallographic analysis revealed a specific orientation relationship between the $MgAl_2O_4$ particles and the Al matrix, denoted as $[2\bar{1}1]_P//[011]_{Al}$ and $(\bar{2}04)_P$/ / $(\bar{1}\bar{1}1)_{Al}$. Based on mismatch calculations, the interface was determined to be semi-coherent. This interfacial structure can act as an additional source of geometrically misfit dislocations, thereby effectively enhancing the work hardening of the material. Additionally, approximately 59 % of the $MgAl_2O_4$ particles were distributed within the grains, with an average size of about 526 nm, which is smaller than that of the particles located at grain boundaries (approximately 906 nm). This combined intragranular and intergranular distribution of particles synergistically pinned the grain boundaries, leading to significant grain refinement, while the elongation of the material only decreased slightly from 7.5 % to 5.1 %. Que et al. [26] achieved uniform dispersion of naturally formed $MgAl_2O_4$ particles within the matrix of an Al–Mg–Si–Fe–Mn alloy melt by employing high-intensity shear processing. The experimental results demonstrate that after shear treatment, the average grain size of α-Al was significantly refined from 423 μm in the untreated specimen to 151 μm. The study indicates a distinct crystallographic orientation relationship between the dispersed $MgAl_2O_4$ particles and the α-Al matrix, specifically expressed as $(\bar{1}1\bar{1})_{Al}$/ /$(2\bar{2}2)_P$ and $[\bar{1}10]_{Al}//[\bar{1}10]_P$. This confirms that $MgAl_2O_4$ particles can act as effective heterogeneous nucleation sites for α-Al, thereby promoting grain refinement. Moreover, the formation of this orientation relationship is also modulated by the presence of other alloying elements. Kumar et al. [27] in situ synthesized nano-sized $MgAl_2O_4$ particles in an Al–Mg–SiO_2 system via an ultrasonic-assisted stir-casting process to reinforce an Al–2Mg–1Si alloy. The study revealed that the α-Al grain size decreased continuously with increasing $MgAl_2O_4$ particle content. When the volume fraction of $MgAl_2O_4$ reached 2 vol%, the mechanical properties of the composite achieved their optimum values, with hardness and tensile strength increasing by 82.6 % and 46.0 %, respectively, while no reduction in elongation was observed. Chen et al. [23] synthesized $MgAl_2O_4$ and Al_2O_3 particle co-reinforced Al–Mg composite by in-situ reactions (1) and (2) in melts and using CuO powder as oxygen source.

$$4Al + 3CuO + Mg = 2Al_2O_3 + MgAl_2O_4 + 3[Cu] \quad (1)$$

$$8Al + 3Cu_2O + 2Mg = 4Al_2O_3 + 2MgAl_2O_4 + 6[Cu] \quad (2)$$

The optimal process parameters with high nucleation rate are: CuO particle size of 5 μm, stirring temperature of 675 °C, CuO content of 0.15 wt%, and Mg content of 1 wt%. The ultimate tensile strength, elongation, and elastic modulus of Al–Mg alloy were increased by 20.1 %, 28.9 %, and 14.4 % respectively. This study indicates that the Mg content and temperature of melt have the greatest influence on the heterogeneous nucleation rate of Al grains. Raghu et al. [28] synthesized $MgAl_2O_4$ particles in situ by introducing a boric acid precursor into an Al-4 wt% Mg melt. These particles exhibited a uniform distribution within the matrix, with an average size of approximately 350 nm. The addition of $MgAl_2O_4$ particles reduced the grain size of the matrix alloy by a factor of 3–4, while the tensile strength of the composite increased by 30 MPa compared to that of the base alloy, along with the retention of 85 % elongation.

Al-2 wt% Fe alloy is a near-eutectic alloy, which has a good casting property and is an important engineering material in fabrication of heat sinks, cover of electric wires, sheet of carriage body, etc. However, the refinement of microstructure and strengthening of Al matrix depending on alloying methods are limited as mentioned above; the ectogenic particle reinforced composites always have shortage of low plasticity.

These studies demonstrate that in-situ-formed $MgAl_2O_4$ particles can effectively refine the microstructure and significantly enhance the mechanical performance of various Al-based alloys, while also imparting superior heat and wear resistance owing to the intrinsic stability of the spinel phase. However, such in situ $MgAl_2O_4$ reinforcement strategies have rarely been explored in Al–Fe alloys, particularly in the near-eutectic Al–2Fe system.

Therefore, the present study employed the in-situ reaction technology to fabricate a $MgAl_2O_4$ particle-reinforced Al–2 wt% Fe based composite through reactions of Fe_2O_3 powder in Al–Mg melts. The formation process of $MgAl_2O_4$ particles and the morphology, size, distribution, and microstructure of $MgAl_2O_4$ particles were analyzed, and their effects on microstructure and mechanical properties of composite were fully investigated, resulting in that the in-situ-generated $MgAl_2O_4$ particles greatly refine the microstructure and improve the mechanical properties of the alloy.

2. Materials and methods

2.1. Raw materials

The raw materials included industrial-grade Al ingot (Al ≥ 99.7 wt%, Fe ≤ 0.12 wt%, Baotou Aluminum Ltd, China), Fe_2O_3 powder (Fe_2O_3 ≥ 99.9 wt%, average size of 0.5 μm, Beasley New Materials Ltd., China), and Mg–10Al master alloy (self-made). The composition of raw materials was designed as Al-3.0 wt% Fe_2O_3-0.9 wt% Mg, accounting for losses of 6.4g of Mg and 2.4g of Fe_2O_3 during melting. The actual amounts of raw materials are shown in Table 1. Theoretically, 1.9 wt% $MgAl_2O_4$ and 2.0 wt% [Fe] can be obtained at the present composition by calculation according to Eq. (3).

$$6Al_{(L)} + 3Mg_{(L)} + 4Fe_2O_{3(S)} = 8[Fe] + 3MgAl_2O_{4(S)} \quad (3)$$

Table 1
Theoretical and actual amounts of raw materials.

Raw materials	Theoretical (g)	Actual (g)
Fe_2O_3	28.6	30.0
Mg–10Al master alloy	3.6	10.0
Pure Al	967.8	967.8
Total	1000	1007.8

2.2. Preparations

967.8 g of Al ingot was melted at 780 °C, and 10.0 g of Mg–Al master alloy was added to form Al–Mg melts. 30.0 g of Fe_2O_3 powder was preheated to 300 °C. The melt was stirred at 300 rpm using stainless steel blades coated with AlN. The temperature of melts was decreased to 700 °C to enhance its viscosity and thereby facilitate the incorporation of the powders into the melt. The preheated Fe_2O_3 powder was then introduced into the vortex of melts. After finished addition of the powders, an asbestos plate was covered on the top of furnace to avoid contacting of the melts to air. The temperature was then increased to 900 °C at a rate of 30 °C/min and held for 25 min in stirring. During this process, much less slag film was observed on the surface of melts, which manifests the oxidation of melts was not serious and the powder was effectively incorporated into the melts. 33.0 g Na_3AlF_6 powder was added to eliminate slag and unreacted Mg ($2Na_3AlF_6 + 3Mg = 6NaF + 2Al + 3MgF_2$). When the temperature decreased to 750 °C, the melt was poured into a steel mold preheated to 200 °C to produce cylindrical samples with a diameter of 15.0 mm. An Al-2 wt% Fe alloy reference was prepared using the same conditions without adding any powder. The chemical composition of both products (Table 2) was analyzed using a direct-reading spectrometer (Equis T4, Wuxi Jiebo Tech. Co.). The contents of Fe and Mg prove the products to meet the chemical composition of Al–2Fe alloy.

2.3. Characterizations

The phase composition of samples was analyzed using an X-ray diffractometer (XRD, D/MAX-2500/PC, Rigaku), with a scanning speed of 3°/min and CuKα target. The microstructure was characterized by a scanning electron microscope (SEM, SU-8220, Hitachi), equipped with an energy-dispersive spectrometer (EDS, X-MaxN, Oxford); the surface of samples was coated with Pt using an ion sputtering coater (JFC-1600, Hitachi); especially, the samples for analysis of $MgAl_2O_4$ particles were deeply etched by a solution of 2 mL HF + 6 mL HNO_3 + 92 mL H_2O for 60 s to fully exposing the three-dimensional morphology. The morphology of Al grains was also characterized using a polarized microscope (DM4P, Leica) to show the refinement effect; the samples were treated by an anodic oxidation (HBF_4 solution, at 20 V for 120 s). The statistical analysis of the sizes of Al grains, $MgAl_2O_4$ particles, and Al_3Fe phases were conducted using an Image-J image software against 5–10 randomly selected SEM images. A transmission electron microscope (TEM, Talos F200X, Thermo Fisher Scientific) was used to characterize the interfacial structure of $MgAl_2O_4$ to Al and Al_3Fe crystals.

Mechanical properties of samples were tested using a universal testing machine (5982, Instron) at a loading speed of 1.5 mm/min. The hardness was inspected by a Vickers hardness tester (FM-810, Future-Tech) using a quenched steel ball indenter with a diameter of 5.0 mm and a pressure of 250 g for 15 s. Five samples were used for each group to obtaining the average of properties.

Table 2
Main chemical composition of both products, wt%.

Materials	Fe	Mg	Si	Al
Composite	1.96	0.12	0.08	Bal.
Al-2 Fe alloy	1.92	–	0.06	

3. Results

3.1. Evolution of microstructure of particle zone in reactions

Fig. 1 shows the microstructure of a particle zone at a reaction time of 5 min. It is evident that Mg, Al, and O elements enriched at the reaction boundary between Al melts and Fe_2O_3 particles. In particular, the Mg concentration is higher than that in the melt but lower than that of Al (Fig. 1c and d). Moreover, Fe is absent in this interfacial region, indicating that Mg and Al have diffused into the Fe_2O_3 particle zone. These indicate that Mg had stronger adsorption affinity to Fe_2O_3 particles than Al elements.

Al elements formed a concentration gradient of decreasing from melts to particle zone; while Mg elements yielded concentration gradients of increasing from the melts to reaction boundary and then decreasing from the reaction boundary to particle zone. The adsorbed elements ignited the reaction to Fe_2O_3, which made it decompose to discharge out O elements rather than Fe; the gradients necessitate the elements enter Fe_2O_3 particle zone to sustain the reactions towards $MgAl_2O_4$.

At the reaction time of 10 min, the particle zone evolved into a dense body from its initial morphology (Fig. 2a), and become enriched in Al and Mg elements (Fig. 2d), indicating that Al and Mg completely diffuse into this zone. Numerous particles with size of about 0.1 μm were dispersively formed on the Al substrate (Fig. 2b). and contained Al, Mg, Fe, and O elements (Fig. 2c), indicating the formation of spinel structure of $(MgFe)Al_2O_4$, an interphase of $MgAl_2O_4$.

At the reaction time of 20 min, the liquid channels were produced in the body as indicated by green arrow (Fig. 3a) because it was composed of Al, Mg, Fe elements and a small amount of O (Fig. 3c). Occurrence of O elements in the liquid channel is due to that the liquid may include the unreacted Fe_2O_3 particles or O^{2-} discharged into the channels, moreover, the spot of electronic beam involved the neighbour Fe_2O_3 particles. The liquid channels cracked the body and connected it to the surrounding melt, which is expected to promote the decomposition of the body as the reaction time increase. The edge of the body (boundary) was also loosed and the $MgAl_2O_4$ particles with size of less 1.0 μm occurred (Fig. 3b and e). In addition, the Al–Fe phase was presented in the Al matrix (Point B, Fig. 3d). These observations suggest that the composite is formed through gradual decomposition of the reaction zone, concurrent formation of spinel particles within both the body and its boundaries.

3.2. Microstructure and phase composition of composite

3.2.1. Microstructure

Fig. 4a and b displays the microstructure of composite. By consulting to the EDS results (Fig. 4c–e), the phase at Point A (Fig. 4a) corresponded to the Al matrix. Absence of Mg in Al matrix indicates the Mg elements remained in melts to be mostly removed by the purification, which well agreed to the chemical composition (Table 1). The short rod-shaped phase at Point B (Fig. 4a) shows an atomic ratio of Al to Fe of approximately 3:1, corresponding to Al_3Fe. (Fig. 4d). Meanwhile, fine granular phases dispersed in the matrix (Fig. 4b) are enriched in O, Al, and Mg with an atomic ratio of ~4:2:1 (Point C in Fig. 4e), indicating the formation of $MgAl_2O_4$ particles. This confirms that the Al–2Fe alloy contained the $MgAl_2O_4$ particles.

3.2.2. Phase composition

Fig. 5 presents the X-ray Diffraction (XRD) patterns of the Al–2Fe-based composite and Al–2Fe alloy (Reference). For both samples, the dominant diffraction peaks can be indexed to Al (PDF# 04-003-1376), indicating that Al remains the primary matrix phase. In the Al–2Fe alloy (Fig. 5b), several additional peaks corresponding to the $Al_{13}Fe_4$ intermetallic phase (PDF# 00-050-0797) are clearly observed, confirming the formation of Fe-rich intermetallics in the alloy.

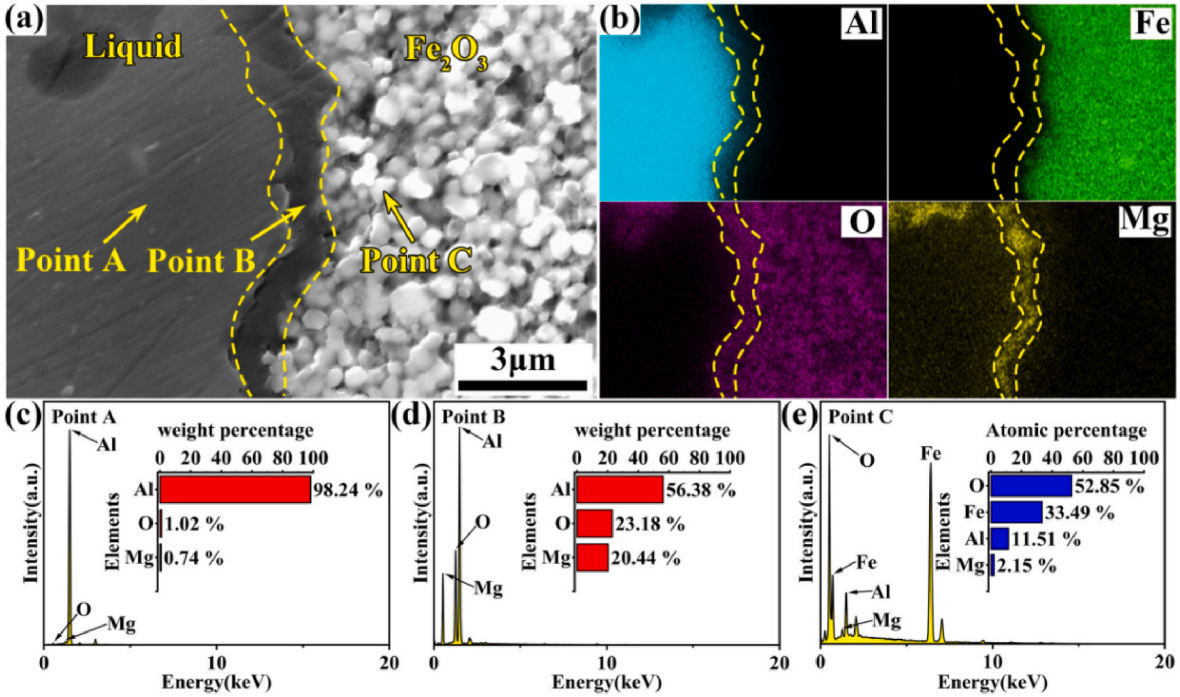

Fig. 1. Microstructure of a reaction zone at reaction time of 5 min. (a) SEM image; (b) EDS mapping; (c–e) EDS results at Points A–C.

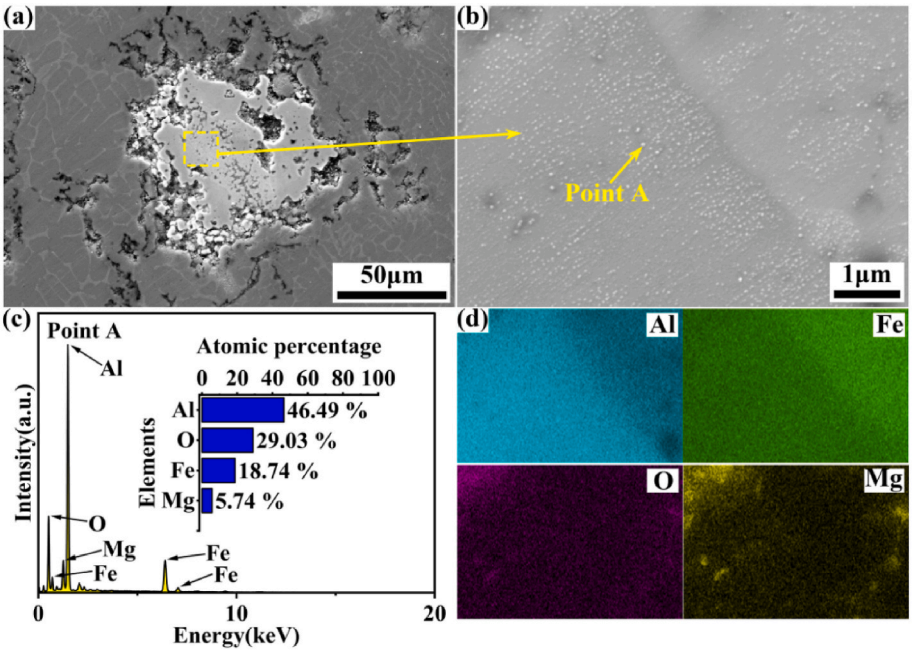

Fig. 2. Microstructure of a reaction zone at reaction time of 10 min. (a) SEM image; (b) Magnification of frame area; (c) EDS result at Point A; (d) EDS mapping of Fig. (b).

In contrast, the XRD pattern of the Al–2Fe-based composite (Fig. 5a) not only shows the diffraction peaks of Al and Al_3Fe (a.k.a. $Al_{13}Fe_4$), but also exhibits extra weak peaks that can be indexed to spinel $MgAl_2O_4$ (PDF# 98-000-0407). This indicates the successful in situ formation of $MgAl_2O_4$ particles in the composite. The relatively low intensity of the $MgAl_2O_4$ peaks suggests that the spinel phase is present in a small amount and/or with fine particle size, which is consistent with the microstructural observations.

No other impurity phases (for example, Fe_2O_3) are detected in either sample, implying that the in-situ reaction proceeds effectively and does not introduce undesirable by-products. These results confirm that the composite consists of an Al matrix reinforced by Al_3Fe intermetallics and in-situ-formed $MgAl_2O_4$ particles When compared to the referenced Al–2Fe alloy (Fig. 5b).

3.3. *Quantitative analysis of morphology and size of phases*

3.3.1. *$MgAl_2O_4$ particles*

The granular $MgAl_2O_4$ particles were uniformly embedded in matrix without distinct aggregation (Fig. 6a), indicating that the in situ reaction

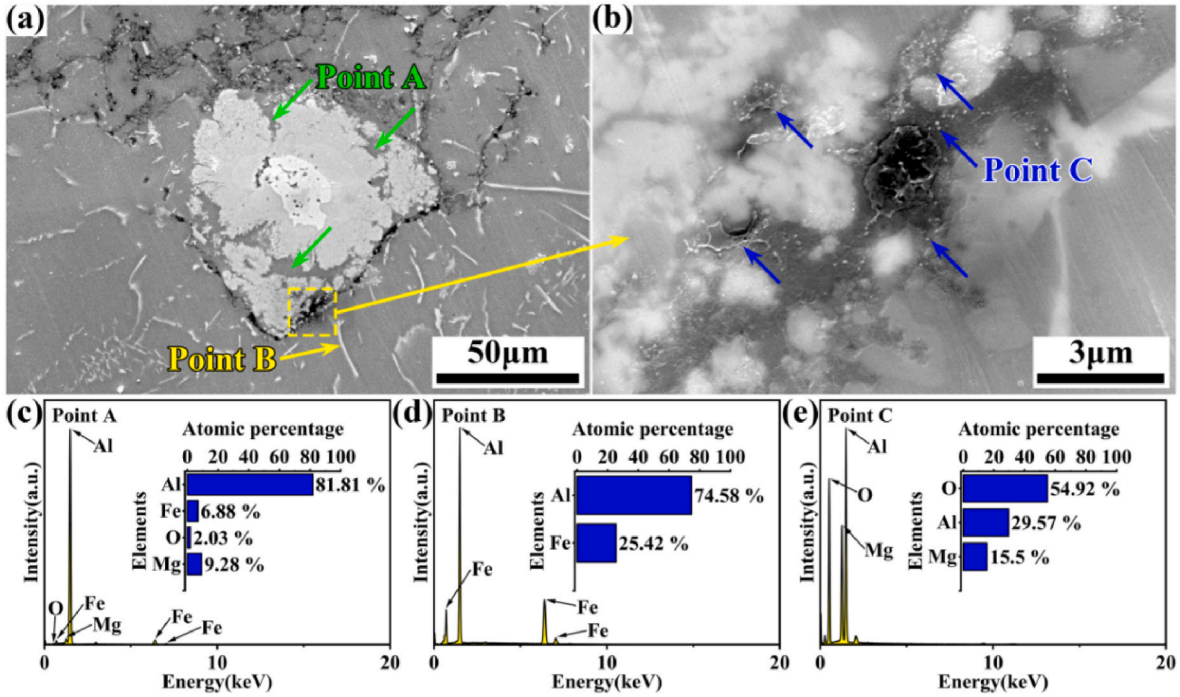

Fig. 3. Microstructure of a reaction zone at reaction time of 20 min. (a) SEM image; (b) SEM image of magnified edge zone; (c) EDS results at Point A (liquid channel); (d) EDS result at Point B (Al_3Fe phase); (e) EDS result at Point C ($MgAl_2O_4$).

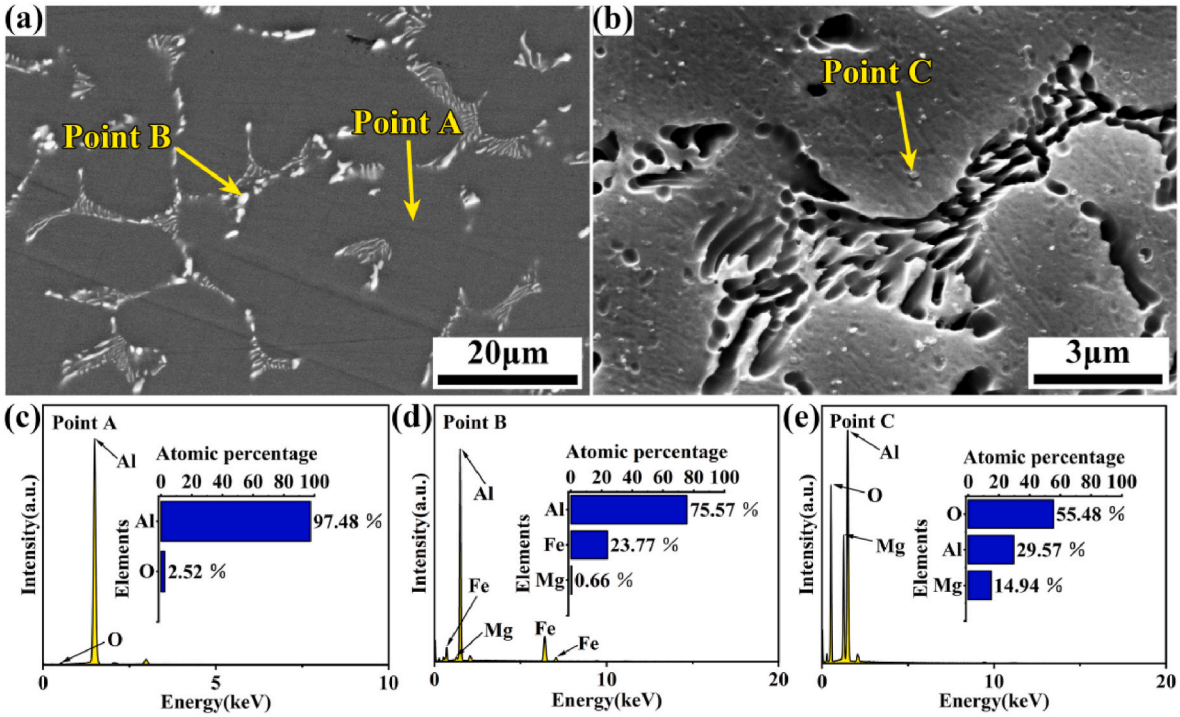

Fig. 4. Microstructure and EDS results of composite. (a) BSE image; (b) Magnification of grain boundary; (c) EDS result at point A (Al matrix); (d) EDS result at point B (Al_3Fe); (e) EDS result at point C ($MgAl_2O_4$).

facilitates a homogeneous dispersion of the reinforcement. The particle size ranged from 0.05 μm to 0.6 μm (Fig. 6b), with an average size (μ_g) of 0.15 ± 0.01 μm. This means that the in-situ produced spinel particles were mostly nano and submicron grades. Such fine crystals are essential to serve as heterogeneous nucleation substrates for refinement of the phases.

3.3.2. *Al grains*

Fig. 7 shows the grain morphology and size distribution of Al in the Al–2Fe alloy and the Al–2Fe-based composite. The Al–2Fe alloy (Fig. 7a) exhibits coarse and irregularly shaped grains with pronounced size inhomogeneity. In contrast, the Al–2Fe-based composite (Fig. 7b) displays much finer and grains with a more uniform distribution throughout the matrix, indicating a significant grain refinement effect induced by the in-

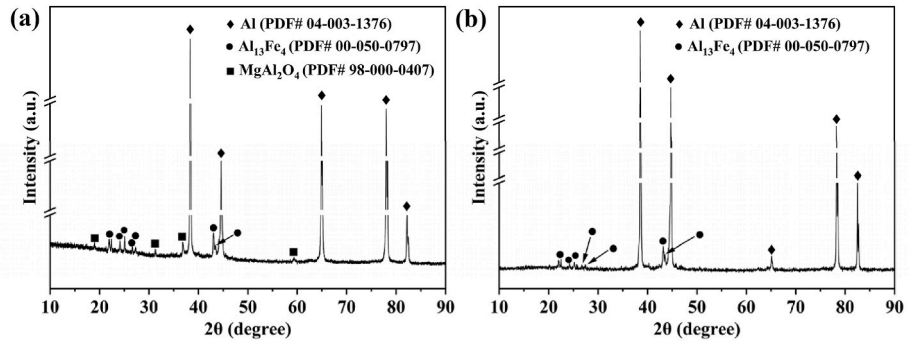

Fig. 5. XRD patterns of samples. (a) Al–2Fe based composite; (b) Al–2Fe alloy.

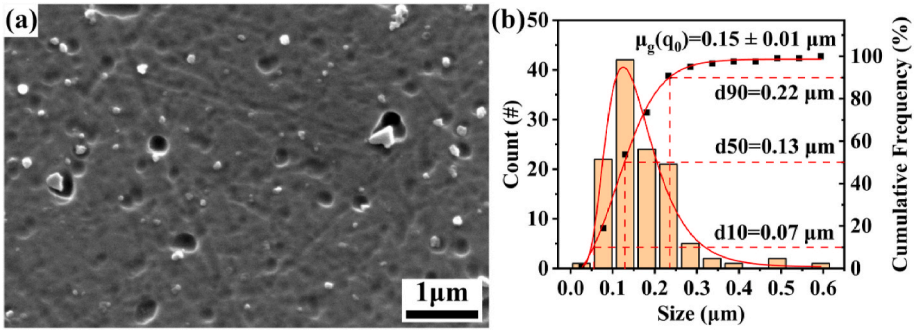

Fig. 6. Morphology and size distribution of $MgAl_2O_4$ particles in composite. (a) Deeply-etched morphology of particles; Notably, some of the particles were lost by wearing and deep etching during the preparation of samples (b) Size distribution was obtained by analyzing totally 133 particles from 10 pictures.

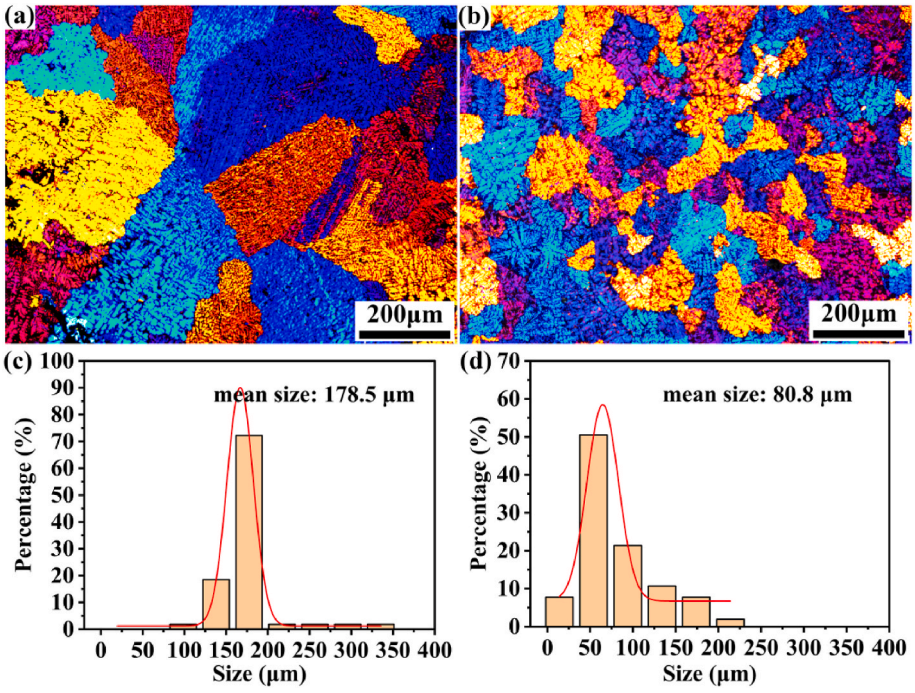

Fig. 7. Morphology and size distribution of Al grains. (a and c) Al–2Fe alloy; (b and d) Al–2Fe based composite.

situ formed $MgAl_2O_4$ particles. The corresponding grain size distributions are shown in Fig. 7c and d. For the Al–2Fe alloy, the grain sizes are mainly distributed in the range of 125–200 μm, with an average size of 178.5 μm. After the introduction of $MgAl_2O_4$ particles, the average grain size of the composite is markedly reduced to 80.8 μm, and the distribution shifts toward smaller sizes, with most grains below ~100 μm. This corresponds to a grain size reduction of approximately 54.7 %.

Such pronounced refinement of Al grains can be attributed to the uniformly dispersed nano and submicron $MgAl_2O_4$ particles, which act as effective heterogeneous nucleation sites during solidification and simultaneously impede grain growth through a pinning effect. The refined grain structure is expected to contribute significantly to the

improved mechanical properties of the Al–2F alloy composite.

3.3.3. Al_3Fe phases

The Al_3Fe phases in both samples are mainly distributed along the Al grain boundaries and appear in various morphologies, including needle, rod, eutectics, and particles. (Fig. 8a and b). In the Al–2Fe alloy (Fig. 8a), coarse needle-like Al_3Fe phases are prevalent, forming a partially continuous network along grain boundaries, which is detrimental to mechanical performance. In contrast, the composite (Fig. 8b) exhibits a much lower fraction of needle-like Al_3Fe phases, which is shorter, finer, and more uniformly dispersed compared to that of the Al–2Fe alloy. By further referring to the statistic results for the geometric parameters of Al_3Fe phases (Fig. 8c and d), it is found that the size of Al_3Fe phases ranged from 0.5 μm to 3.1 μm (average: 2.9 μm) and from 0.5 to 1.6 μm (average: 1.9 μm) respectively, the average size was reduced by 34.5 % when comparing to those of alloy. This information more clearly demonstrates that introduction of the in-situ $MgAl_2O_4$ particles significantly reduced the size and increased the distribution uniformity of Al_3Fe phases.

3.4. Interfacial structure of $MgAl_2O_4$–Al_3Fe and $MgAl_2O_4$–Al

3.4.1. $MgAl_2O_4$–Al_3Fe

The interfacial structure of $MgAl_2O_4$–Al_3Fe, which are critical to the compatibility with the α-Al matrix, were further investigated by transmission electron microscopy (TEM). The TEM image in Fig. 9a reveals that the $MgAl_2O_4$ particles are embedded in the Al matrix and are in direct contact with Al_3Fe phases, which were identified by EDS mapping result (Fig. 9b). Particularly, the highly-crystallized $MgAl_2O_4$ particles exhibited flat and straight interface with Al_3Fe (Fig. 9c), indicating a well-defined interfacial structure. The lattice fringes across the interface are continuous without obvious amorphous layers or interfacial defects, suggesting a good atomic matching between the two phases. In addition, the $MgAl_2O_4$ had a face-centered cubic structure under the observation direction of [112] (Fig. 9d), which provided a coherent relationship of $(115)_{Al_3Fe}//(\bar{1}3\bar{1})_{MgAl_2O_4}$ for Al_3Fe (Fig. 9c); the lattice mismatch was calculated to be 2.8 %. Such a small lattice mismatch and the formation of a semi-coherent interface indicate that $MgAl_2O_4$ particles can effectively act as heterogeneous nucleation substrates for the Al_3Fe phase during solidification. The presence of this crystallographic compatibility significantly reduces the nucleation energy barrier for Al_3Fe, thereby promoting its nucleation on $MgAl_2O_4$ surfaces and suppressing the formation of coarse needle-like Al_3Fe.

Notably, to the best of our knowledge, this is the first experimental evidence revealing a direct crystallographic orientation relationship between in-situ formed $MgAl_2O_4$ particles and Al_3Fe in Al–Fe-based systems. This finding provides new insight into the refinement mechanism of Al_3Fe phases induced by $MgAl_2O_4$ and highlights the unique role of in situ spinel particles in tailoring the interfacial structure and microstructural evolution of Al–Fe composites.

3.4.2. $MgAl_2O_4$–Al

In addition to the interfacial structure of $MgAl_2O_4$–Al_3Fe, $MgAl_2O_4$–Al interface was detailed explored. $MgAl_2O_4$ particles with submicron (at points A) and nanoscale (at point B) in Fig. 10a were identified by EDS mapping (Fig. 10b–d). Regarding the submicron $MgAl_2O_4$ particle at Point A, no crystallographic orientation relationship existed between the submicron $MgAl_2O_4$ and Al although their interface was straight (Fig. 10e), suggesting that this interface is essentially incoherent and that such submicron $MgAl_2O_4$ particles are unlikely to serve as effective heterogeneous nucleation substrates for α-Al. In contrast, the nanoscale $MgAl_2O_4$ exhibited 'cube-on-cube' orientation relationships to Al under observing direction along $[11\bar{2}]$ axis (Fig. 10f), which were $(\bar{1}\bar{1}\bar{1})_{Al}//(\bar{2}\bar{2}\bar{2})_{MgAl_2O_4}$, $(1\bar{3}\bar{1})_{Al}//(2\bar{6}\bar{2})_{MgAl_2O_4}$, and $(2\bar{2}0)_{Al}//(4\bar{4}0)_{MgAl_2O_4}$ in the FFT patterns (Fig. 10g and h). The lattice mismatch was calculated to be 0.17 %, 0.16 %, and 0.21 %, respectively, indicating an nearly perfect lattice matching between α-Al and $MgAl_2O_4$ at the nanoscale. Such extremely small lattice mismatches imply the formation of a highly coherent interface, which significantly lowers the interfacial energy and nucleation barrier for α-Al. Therefore, the nanoscale $MgAl_2O_4$ particles can act as highly effective heterogeneous nucleation sites for Al during solidification, whereas the larger submicron particles, despite forming straight interfaces, lack crystallographic matching and thus do not contribute to Al nucleation. These results provide direct atomic-scale evidence that the nucleation potency of $MgAl_2O_4$ is strongly size-dependent, with only nanoscale spinel particles exhibiting the crystallographic compatibility required for promoting α-Al nucleation. This finding further explains the pronounced grain refinement

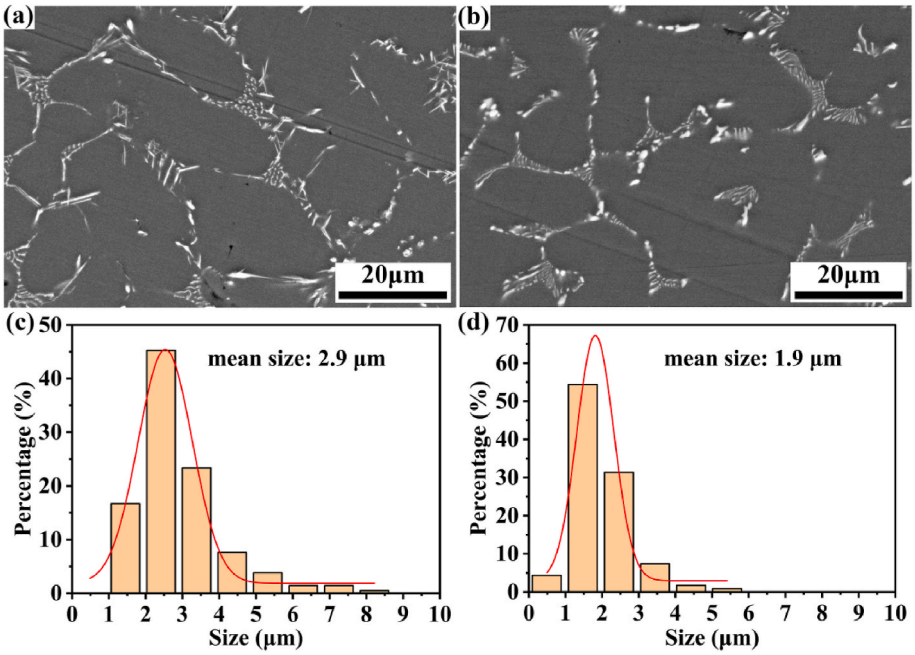

Fig. 8. Microstructure and size distribution of Al_3Fe phases. (a and c) Al–2Fe alloy; (b and d) Al–2Fe based composite.

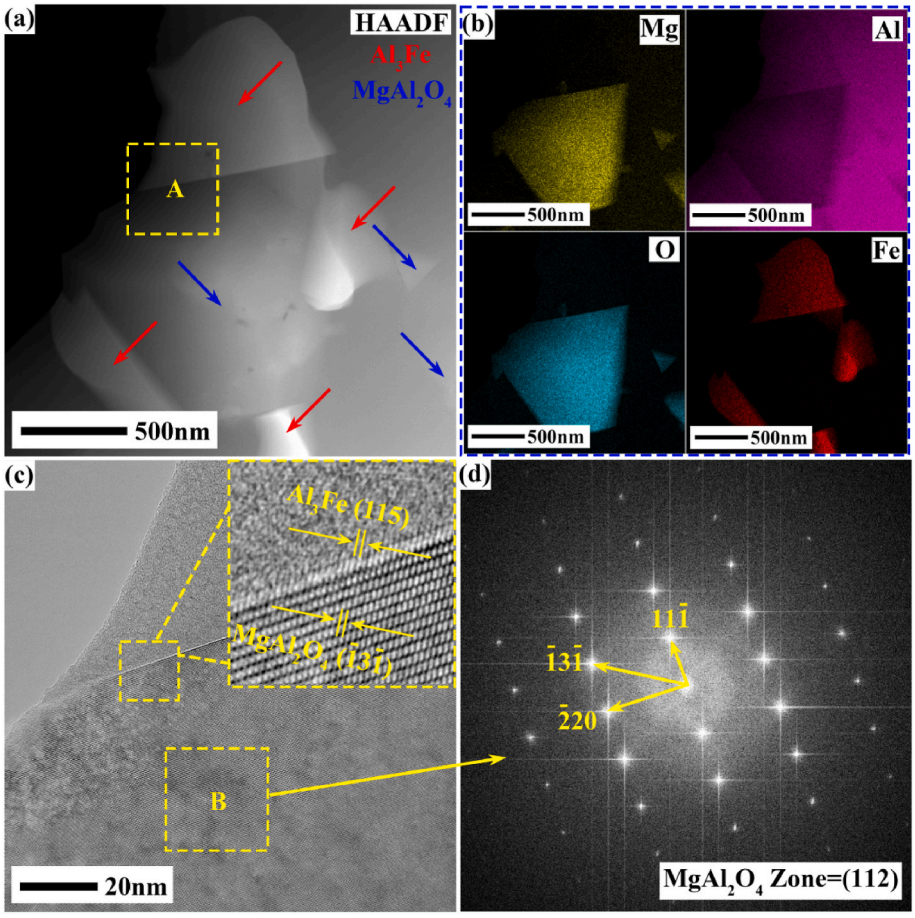

Fig. 9. TEM image of $MgAl_2O_4$–Al_3Fe interface. (a) High-Angle Annular Dark-Field (HAADF) image; (b) Energy-Dispersive X-ray Spectroscopy (EDS) maps, elements identities are unambiguously confirmed by the corresponding EDS elemental maps of O, Mg, Fe, and Al; (c) High-Resolution Transmission Electron Microscopy (HRTEM) image of the $MgAl_2O_4$–Al_3Fe interface; (d) Fast Fourier Transform (FFT) pattern.

observed in the composite and highlights the critical role of in situ generated nanoscale $MgAl_2O_4$ in tailoring the solidification microstructure.

3.5. Mechanical properties of composite and alloy

3.5.1. Strengths

The stress-strain curves of samples are shown in Fig. 11a. A distinct sawtooth-like flow was observed during the plastic deformation stage of the composite, in contrast to the smooth flow behavior of the alloy. This phenomenon is known as the Portevin-Le Chatelier (PLC) effect [29,30], which raises from the periodic interaction between dislocations and hard particles in Al grains. Fig. 11b summarizes the mechanical properties of the materials. The composite exhibit a yield strength (YS) of 77.8 MPa and an ultimate tensile strength (UTS) of were 77.8 MPa, which represent significant increases of 36.9 % and 47.7 %, respectively, compared with those of the Al–2Fe alloy (YS: 56.8 MPa and UTS: 113.6 MPa). Although the elongation decreases from 16.5 % for the alloy to 13.0 % for the composite, this value still indicates sufficient ductility, confirming that the composite remains a plastically deformable material suitable for subsequent forming and processing.

The plastic property of the Al–2Fe based composite was further explored. It can be clearly seen that both the Al–2Fe alloy and the Al–2Fe based composite display dimpled fracture morphologies characteristic of plastic fracture mode. The average size of dimples was measured to be 10.2 μm and 5.6 μm (Fig. 12), manifesting the in-situ generated $MgAl_2O_4$ particles refines the microvoid structure and increases the strength of the matrix, thereby moderately reducing the ductile fracture tendency while retaining overall plastic fracture behavior.

3.5.2. Hardness

Beyond strengths, the hardness is also evaluated. The average hardness of the Al–2Fe alloy is 84.4 HV, whereas that of the Al–2Fe based composite significantly increases to 118.6 HV. This corresponds to an enhancement of approximately 40.5 % upon the introduction of in situ formed $MgAl_2O_4$ particles. The relatively small scatter of the measured values indicates good reproducibility and a homogeneous microstructure in both samples.

The significant increase in hardness can be attributed to the combined effects of grain refinement of the Al matrix, refinement of the Al_3Fe phases, and the dispersion strengthening provided by the uniformly distributed $MgAl_2O_4$ particles, which effectively impede dislocation motion and enhance resistance to plastic deformation.

4. Discussions

4.1. Formation of spinel particles in in-situ reactions

4.1.1. Thermodynamic analysis

The possible reactions in Al–Mg–Fe_2O_3 system are represented by thermodynamic equations (4)–(8):

$$12Al_{(L)} + 6Mg_{(L)} + 8Fe_2O_{3(S)} = 10[Fe] + 6(MgFe)Al_2O_{4(S)} \quad (4)$$

$$2Al_{(L)} + Fe_2O_{3(S)} = 2[Fe] + Al_2O_{3(S)} \quad (5)$$

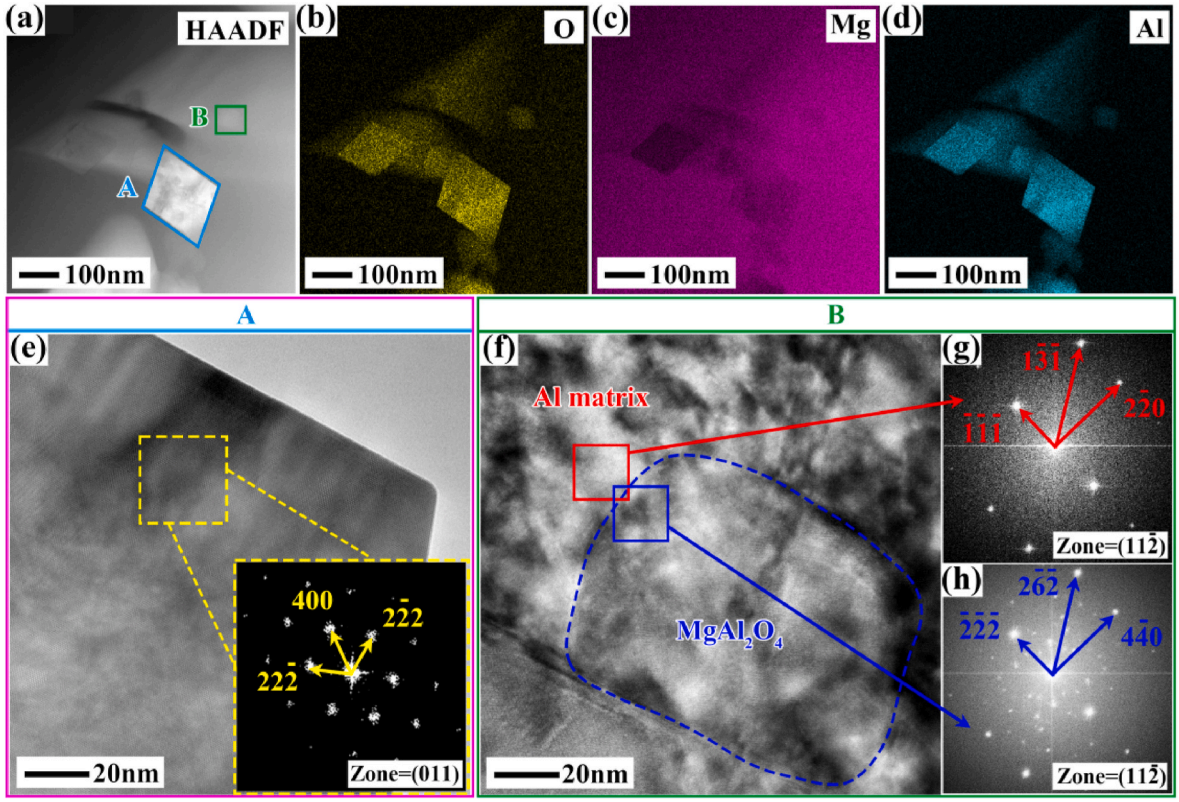

Fig. 10. HRTEM image of $MgAl_2O_4$–Al interface. (a) HAADF image; (b)–(d) EDS mapping, elements identities are unambiguously confirmed by the corresponding EDS elemental maps of O, Mg, and Al; (e) and (f) HRTEM images; (g) and (h) FFT patterns.

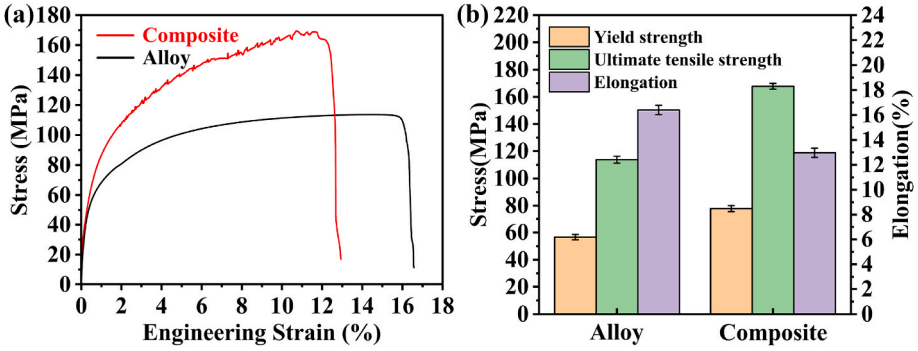

Fig. 11. Tensile stress-strain curves of the Al–2Fe alloy and Al–2Fe based composite. (a) Stress-strain cures; (b) Mechanical properties.

$$3Mg_{(L)} + Fe_2O_{3(S)} = 2[Fe] + 3MgO_{(S)} \quad (6)$$

$$4Fe_2O_{3(S)} + 6Al_{(L)} = 5[Fe] + 3FeAl_2O_{4(S)} \quad (7)$$

$$6Al_{(L)} + 3Mg_{(L)} + 4Fe_2O_{3(S)} = 8[Fe] + 3MgAl_2O_{4(S)} \quad (8)$$

The Gibbs free energy (ΔG_T^{Θ}, kJ/mol) of reactions are expressed by equations 9–13 according to thermodynamic data in literature [31]:

$$\Delta G_5^{\Theta} = -703.47 + 0.06T \quad (9)$$

$$\Delta G_4^{\Theta} = -847.46 + 0.08T \quad (10)$$

$$\Delta G_3^{\Theta} = -1017.62 + 0.10T \quad (11)$$

$$\Delta G_2^{\Theta} = -2681.83 + 0.20T \quad (12)$$

$$\Delta G_1^{\Theta} = -3739.11 + 0.34T \quad (13)$$

The Gibbs energy of reactions remain negative over the practical temperature range, indicating that these reactions are spontaneous process thermodynamically. At 900 °C, the standard Gibbs free energy changes (ΔG_T^{Θ}) are −649.5 kJ/mol, −77.1 kJ/mol, −926.8 kJ/mol, −2500.6 kJ/mol, and −3434.8 kJ/mol for the formation of (MgFe)Al_2O_4, Al_2O_3, MgO, $FeAl_2O_4$, and $MgAl_2O_4$, respectively. Notably, the $MgAl_2O_4$ is the thermodynamically stable phase among the products owing to its lowest free energy; consequently, any interphase are expected to be progressively converted into $MgAl_2O_4$ in the reaction particle zone or the melt given sufficient reaction time under dynamic conditions.

4.1.2. *Reaction process*

Formation process of $MgAl_2O_4$ is mainly governed by diffusion of atoms and ions [25], specifically in this case, it is the diffusion of Al and

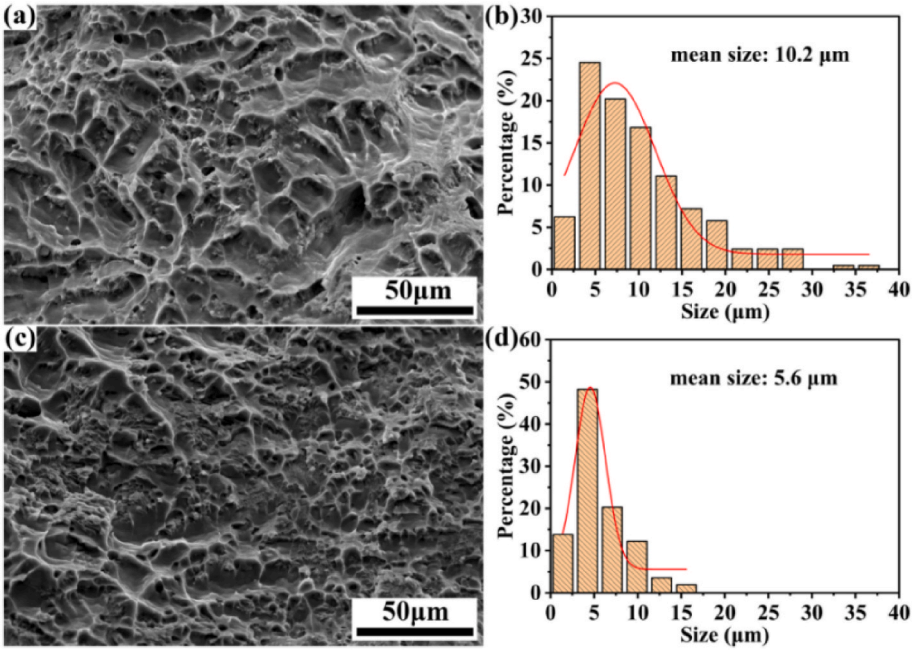

Fig. 12. Fracture morphology of samples. (a and b) Al–2Fe alloy; (c and d) Al–2Fe based composite.

Mg into Fe_2O_3 particles as indicated in Fig. 14. The adsorption of Mg and Al on surface of Fe_2O_3 particles plays a key role in stimulating the reactions leading to the formation of $MgAl_2O_4$. As observed in the interfacial region (Fig. 1), Mg exhibits a higher adsorption ability than that of Al (Fig. 1). This behavior arises because adsorption is a thermodynamically spontaneous process, and Mg acts as a more "surface-active element" than Al. Consequently, Mg adsorption significantly reduces the interfacial energy between the melts and oxides, thereby facilitating interfacial reactions and subsequent spinel formation [32,33]. In addition, Mg has a lower electronegativity than Al, leading to a stronger electrostatic attraction of Mg^{2+} and O^{2-} than between Al^{3+} and O^{2-}. This facilitates the preferential adsorption of Mg^{2+} on on the surface of Fe_2O_3 particles.

The adsorbed Mg species initially react with Fe_2O_3 to form a MgO thin layer with a loose structure. Certainly, it is possible to form (MgFe)O_3 with an insufficient substitution of Mg for Fe. Subsequent reactions between Al and MgO, (MgFe)O_3, and residual Fe_2O_3 progressively disrupt this layer and lead to the formation of intermediate spinel phases, including (MgFe)Al_2O_4 and $FeAl_2O_4$, as well as the eventual product $MgAl_2O_4$ (Fig. 2). These reactions continuously consume Mg and Al, thereby driving fresh Mg and Al diffuse into the contacting zone to sustain the reactions [33,34]. Owing to its lowest (ΔG_T^{Θ} of $MgAl_2O_4$, these interphases are thermodynamically driven to further transform into the most stable $MgAl_2O_4$ through continuous replacements of Mg and Al for Fe in the particle zone and melts. Meantime, the discharged Fe atoms from the Fe_2O_3 tend to aggregate as particles at the boundary of Fe_2O_3 particles to minimize their interfacial energy [35].

Afterwards, Al and Mg gradually enrich in the Fe-rich regions, resulting in formation of low-melting-point Al–Mg–Fe micro melts that propagate from the outer surface toward the interior. (Fig. 3). The micro melts extend inwards to form the branched melts channels, which facilitate the transportation of Al and Mg because diffusion in liquid is faster than in solid [36,37]. The melts channels separate the densified particle zone, which eventually collapses under the continuous reactions and mechanical stirring. Thus, the particle-like products are involved into the melts and dispersed by the continuous stirring [38]. Given the abundance of Al and Mg in the melts, the interphases of (Mg,Fe)Al_2O_4, $FeAl_2O_4$, Al_2O_3, and MgO, even formed, will be converted into $MgAl_2O_4$ in the melts by further elemental substitutions. Meanwhile, the liberated Fe species dissolve into the melt and subsequently participate in forming the Al–Fe matrix of the composite during solidification [39]. This deduction was confirmed by the phase composition (Fig. 4) and microstructure (Fig. 5) of the composite, in which the Al, Al_3Fe, and $MgAl_2O_4$ phases are found to coexist.

4.2. Refinement of microstructure

The binary Al–2Fe alloy is a near-eutectic alloy and it is typically composed of coarse α-Al grains and needle/flake-like Al_3Fe phases (Fig. 8a). Refinement of both phases is therefore essential for improving the mechanical performance of the alloy because it can simultaneously enhance the strength and plasticity of the metal materials.

In the present case, the Al_3Fe phases and Al grains were significantly refined by introducing in-situ generated nano-submicron $MgAl_2O_4$ crystals in the melts (Figs. 7 and 8), which acts as the heterogeneous nucleation substrates for Al_3Fe phases and α-Al grains (Figs. 9 and 10). The refinement mechanism of $MgAl_2O_4$ for α-Al grains has been reported in other systems. Wang et al. [40] observed the orientation relationships of $(11\bar{1})_{Al}//(11\bar{1})_{MgAl_2O_4}$ and $(02\bar{2})_{Al}//(11\bar{3})_{MgAl_2O_4}$ between nanosized $MgAl_2O_4$ and Al matrix in the vacuum hot pressing of Al–Mg–B_2O_3 system. Wang et al. [41] found that the submicron $MgAl_2O_4$ provides an orientation relationship of $(04\bar{2})_{Al}//(020)_{MgAl_2O_4}$ to Al crystals in the reactive sintering of Al–Mg–ZnO system. Thakur et al. [42] observed no orientation relationship to exist between the micron $MgAl_2O_4$ particle and Al to occur in the Al–Mg–SiO_2 system through casting route. This indicated that many orientation relationships cam be formed between $MgAl_2O_4$ and Al matrix because they have the same crystal structure and very closed crystal parameter that yield much less mismatch. Moreover, the formation of orientation relationships is strongly size-dependent: the smaller particles, particularly the nanoscale ones, exhibit a greater tendency toward structural compatibility with the coherent or semi-coherent interfaces. This enables them to act as effective heterogeneous nucleation substrates for Al crystals.

Notably, in the present study, three orientation relationships of $(\bar{1}\bar{1}\bar{1})_{Al}//(\bar{2}\bar{2}\bar{2})_{MgAl_2O_4}$, $(1\bar{3}\bar{1})_{Al}//(2\bar{6}\bar{2})_{MgAl_2O_4}$, and $(2\bar{2}0)_{Al}//(4\bar{4}0)_{MgAl_2O_4}$ were identified by the FFT patterns (Fig. 10g and h), which uncovers the new refinement routes by the different orientation

relationships from previous reports. Particularly, for the first time, $MgAl_2O_4$ crystals are experimentally shown to act as the heterogeneous nucleation substrate for Al_3Fe phases by the coherent relationship of $(115)_{Al_3Fe}//(\bar{1}3\bar{1})_{MgAl_2O_4}$.

Moreover, the growth of $MgAl_2O_4$ crystals is effectively resisted in present condition because the Al melts contain only limited amount of O elements and the supply of necessary elements of Al and Mg for crystal growth is disturbed by the stirring [27]. Thus, the majority of spinel particles are retained at small sizes (Figs. 4 and 6).

The in-situ $MgAl_2O_4$ crystals play an intrinsic role in refinements of both Al and Al_3Fe phases because it reduces the nucleation energy by providing the coherent substrates. The stirring makes the particles uniformly disperse in the melts [43], ultimately, obtaining a nano-submicron $MgAl_2O_4$ particle-reinforced Al–2Fe based composite.

Compared with the previously reported $MgAl_2O_4$-reinforced Al-based composites, three differences are identified in the present approach. First, this study reports for the first time that $MgAl_2O_4$ crystals can establish a coherent crystallographic relationship with Al_3Fe phase, enabling their heterogeneous nucleation and refinement. Second, the new coherent orientation relationships between $MgAl_2O_4$ and Al, different from the previous, are uncovered, indicating the strong crystallographic compatibility of $MgAl_2O_4$ with the Al matrix. Third, the reduced Fe elements directly act as the alloying element of Al–Fe alloy, leaving out addition of Fe-containing raw materials. Therefore, introduction of the in-situ $MgAl_2O_4$ particles in Al–Fe alloys provides multiple advantages on the formation and enhancement of the microstructure.

4.3. Strengthening of composite

The coarse Al_3Fe phases and Al grains in Al–2Fe alloy are fatal factors to worsen the strength and plasticity. The effects of grain refinement and phase composition on mechanical properties of alloys are extensively studied. Fine grain together with suitable combination of soft and hard phases are essential for enhancing the strength, plasticity, and hardness simultaneously [44–47]. Grain refinement promotes dislocation movement by providing multiple slip directions; while the increased grain boundary in turn inhibits the dislocation movement by interfacial strengthening. Thus, a suitable combination of soft and hard phases enables more uniform distribution of applied loads, yielding a balance on strength, hardness, and ductility.

In the present case, the in-situ reactions produced fine $MgAl_2O_4$ particles in the alloy, which largely improved the strength and hardness while had less negative influence on plasticity (Figs. 11 and 13). This is because fine spinel particles further realized multi-dimensional refinement and reinforcement effects [48].

(1) Spinel crystals have coherent interfaces to Al_3Fe and Al phases, which strengthen the interfacial combination to reduce the cracking trend along the interfaces under loading [49].

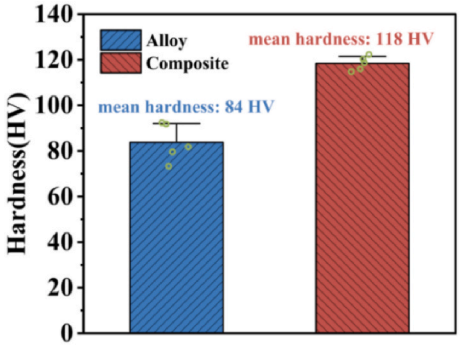

Fig. 13. Hardness values of Al–2Fe based alloy and composite.

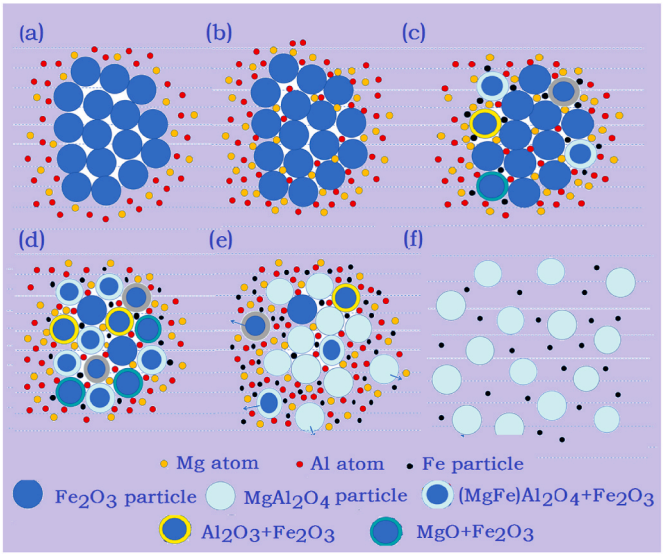

Fig. 14. Sketchmap of the formation process of $MgAl_2O_4$ particles.

(2) The dispersively distributed spinel crystals largely inhibit the movement of dislocations; which strengthens the soft Al matrix [50].

(3) The refined Al grains make dislocations migrate in more slipping directions, which has positive effect on the plastic deformation [51]. Moreover, the refined brittle Al_3Fe phases significantly reduce their segregation effect to Al matrix and the stress concentration at their tips, which delays cracking of the interface. The fine Al_3Fe particles play similar resistant role in dislocation movement as $MgAl_2O_4$ particles [52]. These effects are reflected in the sawtooth fluctuation in plastic deformation by pinning and unpinning of dislocations repeatedly (Fig. 11) [53].

(4) The hard particles of Al_3Fe and $MgAl_2O_4$ result in earlier hardening of Al matrix and accumulation of stress at interfaces to reduce the plasticity [54,55]. However, the finely dispersed $MgAl_2O_4$ particles, refined Al grains and Al_3Fe phases, and coherent interfaces offset the negative effect of hard particles in some extent; therefore, the composite retains good plasticity, with only a slight reduction in elongation

The strengthening effect of Al grain refinement and dislocation (Orowan) on yield strength of materials induced by $MgAl_2O_4$ particles can be calculated using following equations 14–16. The grain refinement-induced strengthening effect ($\Delta\sigma_{HP}$) was calculated using the Hall-Petch relation [56,57]:

$$\Delta\sigma_{HP} = k_y\left(d^{-1/2} - d_0^{-1/2}\right) \tag{14}$$

Where d and d_0 represent the grain sizes of Al in the composite and Al–2Fe alloy respectively (Fig. 7). k_y denotes the Hall-Petch coefficient for Al–Fe alloy [58].

The Orowan strengthening effect ($\Delta\sigma_{Orowan}$) can be calculated using the following equations [59]

$$\Delta\sigma_{Orowan} = \frac{0.8Gb}{\lambda} ln\frac{d}{2b} \tag{15}$$

$$\lambda = d\left[\left(\frac{1}{2f_v}\right)^{1/3} - 1\right] \tag{16}$$

Where G is the shear modulus of the Al matrix, b is the Burgers vector of Al [60]. λ is the interparticle distance; d and f_v represent the average size and volume fraction of $MgAl_2O_4$ particles, which can be estimated from

the distribution and size of $MgAl_2O_4$ particles (Figs. 6 and 8). The values of the parameters were given in Table 3.

The calculated values of $\Delta\sigma_{HP}$ is 15.3 MPa, with the values of $\Delta\sigma_{Orowan}$ is 7.1 MPa; the resulted total contribution (22.4 MPa) is slightly higher than the experimentally measured value (21.0 MPa), which can be attributed to casting defects such as pores formed during high-temperature remelting and mechanical stirring, effects that are not accounted for in the strengthening model and tend to reduce the yield strength. The theoretical calculation confirms that the introduction of $MgAl_2O_4$ particles exactly improved the strength of composite. The strengthening effect of Al_3Fe refinement can not be calculate because the Orowan mechanism is not suitable for large particles more than 1 μm [61]; the present Al_3Fe phases had an average particle size of 5.9 μm.

4.4. Potential application and theoretical contribution of the research

The large-bulk ingots always have coarse microstructure and nonuniform mechanical properties due to the slow solidification rate. Straightening cooling is not effective; advanced techniques such as squeeze casting, semi-solid casting, and spray deposition are not suitable for the fabrication [9–11]. An effective strategy is to modify the melt nature to promote heterogeneous nucleation and thereby refine the microstructure. However, conventional melt modifications with refiners (Al–Ti–B, Al–Ti–C, TiB_2) [3,4] and modifiers of rare earth and other alloying elements [5–8] are not effective on simultaneous enhancement of strength, hardness, and plasticity.

Compositing of aluminum alloy represents an effective technique for improving the mechanical properties of large-bulk alloys. However, ex-situ particle reinforcement, as a conventional compositing method, has a distinct shortage of low plasticity, which is unsuitable for the fabrication of deformable alloy ingots.

In contrast, the present in-situ solid-liquid reaction method demonstrates its advantages in the production of large-bulk alloys because the in-situ-generated spinel particles play an intrinsic role in refinement of microstructure. This self-generated refinement capability depends less on the melts volume and external technical conditions. When compared to the modifications with refiners and alloying elements, the present technique possesses a promising engineering potential for preparation of large-bulk alloys with refined uniform microstructure, and comprehensive mechanical properties. This in-situ liquid-solid reaction method has been applied in other systems. Its effectiveness was confirmed, the grain size was refined (Figs. 7 and 8), the coherent relationships occurred (Figs. 7 and 8), so the mechanical properties were improved (Figs. 11 and 13). Moreover, the obtained composite melts can also be combined into the squeeze casting and semi-solid casting for further improvement of the properties.

Admittedly, industrial implementation is more challenging than laboratory processing as rapid control of melt temperature is difficult and powder addition requires longer processing times. Nevertheless, these challenges are worthwhile to address, given the potential to produce high-quality ingots with superior and uniform properties.

From the formation process and modification mechanism of the composite, it can be recognized that this core technique lies in the coordinated regulation to the nature of alloys in terms of cross-scale (micro-submicro-nano), heterogeneity (spinel ceramic phase, Al_3Fe intermetallics, metal matrix), and interface (coherency), which offers a new paradigm for solving the common contradiction of metallic materials between strengthening and embrittlung.

The core scientific contribution of the research lies in the extension of pursuit from material's homogeneity to heterogeneous system, embodying the overall novelty on concept of materials design. It is helpful to deeply understand the relationship between the materials design, technical implementation, and regulation to material's microstructure and macroscopic properties.

Table 3
The given values of the parameters in equations.

Parameters	Al grains		$MgAl_2O_4$ particles		
	d	d_0	d	f_v	λ
values	178.5 μm	80.8 μm	0.28 μm	1.41 vol %	2.3 μm

5. Conclusions

The spinel ($MgAl_2O_4$) particles reinforced Al–2Fe composite was successfully prepared by the in-situ solid-liquid reactions in Al–1.5 wt% Mg melts by adding 3.1 wt% Fe_2O_3 powder, stirring at 700 °C, reacting at 900 °C for 25 min, and purring at 750 °C.

Formation of the $MgAl_2O_4$ particles is primarily govern by the diffusion of Mg and Al elements and their reactions with Fe_2O_3.

Mg exhibits a stronger adsorption affinity to Fe_2O_3 than Al, which initiates the interfacial reactions to Fe_2O_3; the resulting concentration gradients of Mg and Al continuously sustain the formation of $MgAl_2O_4$.

The reaction pathway involves the sequential transformation of intermediate phases, including MgO and $(MgFe)Al_2O_4$, into the thermodynamically most stable $MgAl_2O_4$ spinel.The initially loose Fe_2O_3 particle aggregations are sintered into a dense entirety, which is then decomposed by formation of liquid channels, leading to the separation of $MgAl_2O_4$ particles and Fe elements.

The in-situ generated spinel particles exhibit excellent crystallinity and nano-micron sizes, which were dispersively distributed in Al matrix.

Nanoscaled spinel crystals have coherent relationships of $(\overline{111})_{Al}//(\overline{222})_{MgAl_2O_4}$, $(1\overline{3}1)_{Al}//(2\overline{6}2)_{MgAl_2O_4}$, and $(2\overline{2}0)_{Al}//(4\overline{4}0)_{MgAl_2O_4}$ for Al and $(115)_{Al_3Fe}//(\overline{1}3\overline{1})_{MgAl_2O_4}$ for Al_3Fe crystals, respectively, enabling $MgAl_2O_4$ to act as effective heterogeneous nucleation substrates for both phases.

The presence of $MgAl_2O_4$ particles leads to pronounced refinement of the α-Al grains and Al_3Fe intermetallics, with average size reductions of 54.7 % and 34.5 %, respectively, compared with the Al–2Fe alloy.

The spinel particle reinforced Al–2Fe composite exhibited excellent mechanical properties, yield strength of 77.8 MPa, tensile strength of 167.8 MPa, hardness of 118.6 HV, and elongation of 13.0 %, corresponding to increases of 36.9 %, 47.7 %, and 40.5 %, respectively, and a only moderate decrease in ductility (−21.1 %).

CRediT authorship contribution statement

Hao Lian: Writing – original draft, Visualization, Software, Investigation, Formal analysis, Data curation. **Z.M. Shi:** Supervision, Resources, Methodology, Funding acquisition, Conceptualization. **Wenlong Yu:** Investigation, Software, Data curation. **Y. Wang:** Software, Methodology. **Wenbin Wang:** Formal analysis, Data curation. **Na Pang:** Data curation, Software.

Confirmation of authorship

The authors declare no conflict of interest in the study; in the collection, analyses, or interpretation of data; in the writing of the manuscript, or in the decision to publish the results.

Each author has his/her individual contribution to the article and all authors have approved the final article.

Declaration of competing interest

The authors declare that they have no known competing financial interests or personal relationships that could have appeared to influence the work reported in this study.

Acknowledgment

This work is supported by the Science and Technology Project of Inner Mongolia, China (Grant No. 2024KJHZ0017) and University Research Project of Inner Mongolia, China (Grant No. NJZY23061).

We would like to appreciate to Dr. Long Zhang, Dr. Tiewu Wang, Dr. Ruofei Zhu, and Dr. Xueping Zhao for their guidance and critical feedback throughout this research.

Data availability

Data will be made available on request.

References

[1] Luo SX, Shi ZM, Li NY, Lin YM, Liang YH, Zeng YD. Crystallization inhibition and microstructure refinement of Al-5Fe alloys by addition of rare Earth elements. J Alloys Compd 2019;789:90–9. https://doi.org/10.1016/j.jallcom.2019.03.071.

[2] Shi ZM, Gao K, Shi YT, Wang Y. Microstructure and mechanical properties of rare-earth modified Al–1Fe binary alloys. Mater Sci Eng, A 2015;632:62–71. https://doi.org/10.1016/j.msea.2015.02.068.

[3] Lapin J, Klimová A, Pelachová T, Štamborská M, Bajana O. Synergistic effect of Ti, B, Si, and C on microstructure and mechanical properties of as-cast Al0.4Co0.9Cr1.2Fe0.9Ni1.2(Si, Ti, C, B)0.375 complex concentrated alloy. J Alloys Compd 2023;934:168050. https://doi.org/10.1016/j.jallcom.2022.168050.

[4] Bian ZY, Cai YL, Zhang DD, Wu YL, Zhao DC, Wang ML, Cui S, Wang HW. Improving mechanical performance of heat-resistant eutectic Al–Fe–Ni alloy by in-situ TiB_2 particles. Mater Lett 2024;358:135857. https://doi.org/10.1016/j.matlet.2023.135857.

[5] Li SX, Jiang HX, Li YQ, Zhang LL, Sun H, He J, Jiang HC, Zhao JZ. Influence of rare Earth cerium on the microstructure and performances of Al–Fe alloy. Sci China Technol Sci 2023;66:3317–27. https://doi.org/10.1007/s11431-023-2468-3.

[6] Qin LM, Tang P, Meng SX. Effect of Ni addition on the microstructure, conductivities and mechanical properties of as-cast Al–Fe alloys. J Alloys Compd 2024;986:174160. https://doi.org/10.1016/j.jallcom.2024.174160.

[7] Chen R, Li ML, Chen BA, Han Y, Zhu ZX, Yang CL, Zheng W, Duo JL. Microstructure, mechanical and electrical properties of Al–Fe–Cu–RE alloy. In: Proceedings of the 11th frontier academic forum of electrical engineering (FAFEE 2024). Singapore: Springer; 2025. p. 547–56. https://doi.org/10.1007/978-981-97-8832-3_55. Chong Qing, China.

[8] Niu XL, Luan ZQ, Mei Y, Yu Y. The corrosion resistance of Al–Fe–Co–Cr–Ni–Cu high entropy alloy coatings. In: Proceedings of the 2023 2nd international conference on applied mechanics and advanced materials (ICAMAM 2023); hybrid. Changsha, China. Bristol, UK: IOP Publishing; 2023, 012023. https://doi.org/10.1088/1742-6596/2535/1/012023.

[9] Hu A, Liu SF, Shen WT, Ying L, Hu H. Nanostructure development of Al–Fe eutectic alloy. Defect Diffusion Forum 2025;439:3–11. https://doi.org/10.4028/p-uRmg49.

[10] Wang X, Guan R-G, Wang Y. Formation mechanism of nanoscale Al_3Fe phase in Al-Fe alloy during semisolid forming process. Metall Mater Trans B 2018;49:2225–31. https://doi.org/10.1007/s11663-018-1323-7.

[11] Vourlias G, Pistofidis N, Pavlidou E, Stergioudis G. Reinforcement of Al–Fe–Ni alloys with the in situ formation of composite materials. J Alloys Compd 2009;483:178–81. https://doi.org/10.1016/j.jallcom.2008.07.173.

[12] Pramod SL, Bakshi SR, Murty BS. Aluminum-based cast in situ composites: a Review. J Mater Eng Perform 2015;24:2185–207. https://doi.org/10.1007/s11665-015-1424-2.

[13] Yang Y, Lan J, Li XC. Study on bulk aluminum matrix nano-composite fabricated by ultrasonic dispersion of nano-sized SiC particles in molten aluminum alloy. Mater Sci Eng A 2004;380:373–8. https://doi.org/10.1016/j.msea.2004.03.073.

[14] Mazahery A, Abdizadeh H, Baharvandi HR. Development of high-performance A356/nano-Al_2O_3 composites. Mater Sci Eng A 2009;518:61–4. https://doi.org/10.1016/j.msea.2009.04.014.

[15] Deng KK, Wu K, Wu YW, Nie KB, Zheng MY. Effect of submicron size SiC particulates on microstructures and mechanical properties of AZ91 magnesium matrix composites. J Alloys Compd 2010;504:542–7. https://doi.org/10.1016/j.jallcom.2010.05.159.

[16] Li Q, Qin F, Dong BX, Geng Run, Lv MM, Zhao QL, Jiang QC. Fabrication, microstructure refinement and strengthening mechanisms of nanosized SiCP/Al composites assisted ultrasonic vibration. Mater Sci Eng, A 2018;735:310–7. https://doi.org/10.1016/j.msea.2018.08.060.

[17] Su H, Gao WL, Feng ZH, Lu Zheng. Processing, microstructure and tensile properties of nano-sized Al_2O_3 particle reinforced aluminum matrix composites. Mater Design 2012;36:590–6. https://doi.org/10.1016/j.matdes.2011.11.064.

[18] Arun J, Ansalam Raj TG, Reby Roy KE, Suresh S. Fatigue life, distortion behavior of AA 8011- nano B_4C composite using simulated acoustic emission technique – an experimental and statistical appraisal. Int J Fatigue 2022;164:107168. https://doi.org/10.1016/j.ijfatigue.2022.107168.

[19] Ranjan S, Jha PK. Investigation on the thermodynamic stability of phases evolved in Al-based hybrid metal matrix composite fabricated using in-situ stir casting route. J Manuf Process 2023;95:14–26. https://doi.org/10.1016/j.jmapro.2023.03.084.

[20] Li GR, Xu T, Wang HM, Zhao YT, Chen G, Kai XZ. Microstructure study of hot rolling nanosized in-situ Al_2O_3 particle reinforced A356 matrix composites. J Alloys Compd 2021;855:157107. https://doi.org/10.1016/j.jallcom.2020.157107.

[21] Li H-T, Wang Y, Fan Z. Mechanisms of enhanced heterogeneous nucleation during solidification in binary Al-Mg alloys. Acta Mater 2012;60:1528–37. https://doi.org/10.1016/j.actamat.2011.11.044.

[22] Li Y, Wang YH, Wang ML, Wang HW, Chen Z. Progress in grain refinement of solidification and development of new grain refiner. Foundry Technol 2023;44:483–98. https://doi.org/10.16410/j.issn1000-8365.2023.3146.

[23] Chen PY. Research on the Preparation of $MgAl_2O_4$/Al composites by Melt reaction and its refining effect. [dissertation]. Qingdao (China). Qingdao University of Science and Technology; 2022.

[24] Dudek HJ, Borath R, Kleine A. Spinel growth in the interface of δ-Al_2O_3 fibre reinforced aluminium piston alloys. J Mater Sci 2004;31:795–805. https://doi.org/10.1007/BF00367901.

[25] Jia LJ, Rong XD, Zhao DD, Zhang X, He CN, Zhao NQ. Microstructural characteristic and mechanical properties of the in-situ $MgAl_2O_4$ reinforced Al matrix composite based on Al-Mg-ZnO system. J Alloys Compd 2021;891:161991. https://doi.org/10.1016/j.jallcom.2021.161991.

[26] Que ZP, Wang Y, Mendis CL. Heterogeneous nucleation of α-Al on naturally formed $MgAl_2O_4$ particles during solidification of Al–Mg–Si–Fe–Mn alloys. Materialia 2020;14:100900. https://doi.org/10.1016/j.mtla.2020.100900.

[27] Kumar TS, Thankachan T, Giri J, Makki E, Dhanasekar R, Guru A. Microstructural characterization of in-situ $MgAl_2O_4$ nanoparticles reinforced Al–2Mg–1Si composite produced using the ultrasonic assisted stir casting process. J Mater Res Technol 2024;29:2458–67. https://doi.org/10.1016/j.jmrt.2024.01.254.

[28] Raghu R, Nampoothiri J, Kumar T. S In-situ generation of $MgAl_2O_4$ particles in Al–Mg alloy using H_3BO_3 addition for grain refinement under ultrasonic treatment. Measurement 2018;129:389–94. https://doi.org/10.1016/j.measurement.2018.07.056.

[29] Liang ZP, Zhang S-L, Guan C, Yin HS, Zhang ZY, Wu J-L, Zhang D-M. Effects of rolling on microstructures and properties of in-situ (TiB_2 + ZrB_2)/AlSi9Cu1 composites. Mater Res Express 2019;6:106584. https://doi.org/10.1088/2053-1591/ab3b36.

[30] Pink E, Kumar S, Tian BH. Serrated flow of aluminium alloys influenced by precipitates. Mater Sci Eng, A 2000;280:17–24. https://doi.org/10.1016/S0921-5093(99)00650-4.

[31] Ye DL, Hu JH. Handbook of practical inorganic thermodynamic data. fourth ed. Beijing: Metallurgical industry press; 2002.

[32] Shinomiya Y, Yamamoto J, Kato K, Ono H, Yamaguchi K, Komori K. Thermodynamics of formation of Al3Fe inter-metallic compound for Fe removal from molten Al-Mg alloy. Mater Trans 2023;64:322–7. https://doi.org/10.2320/matertrans.MT-LA2022025.

[33] Shen P, Zhang LF, Fu JX, Zhou H, Wang Y, Cheng LM. The effect of Al content on the wettability between liquid iron and MgO-Al_2O_3 binary substrate. Ceram Int 2019;45:1287–11295. https://doi.org/10.1016/j.ceramint.2019.02.205.

[34] Carter RE. Mechanism of solid-state reaction between magnesium oxide and aluminum oxide and between magnesium oxide and ferric oxide. J Am Ceram Soc 1961;44:116–20. https://doi.org/10.1111/j.1151-2916.1961.tb13724.x.

[35] Shi QM, Mertens R, Dadbakhsh S, Li GC, Yang SF. In-situ formation of particle reinforced Aluminium matrix composites by laser powder bed fusion of Fe_2O_3/AlSi12 powder mixture using laser melting/remelting strategy. J Mater Process Technol 2022;299:117357. https://doi.org/10.1016/j.jmatprotec.2021.117357.

[36] Xue Y, Shen RJ, Ni S, Song M, Xiao DH. Fabrication, microstructure and mechanical properties of Al-Fe intermetallic particle reinforced Al-based composites. J Alloys Compd 2015;618:537–44. https://doi.org/10.1016/j.jallcom.2014.09.009.

[37] Mei J, Halldearn RD, Xiao P. Mechanisms of the aluminium-iron oxide thermite reaction. Scripta Mater 1999;41:541–8. https://doi.org/10.1016/S1359-6462(99)00148-7.

[38] Shi XW, Nie KB, Deng KK, Xu C. Effect of micro-nano hybrid SiCp on microstructure and mechanical properties of 7075Al alloy. J Mater Res Technol 2024;32:3476–89. https://doi.org/10.1016/j.jmrt.2024.08.118.

[39] Lian H. Improvement of microstructure and properties of Al-Fe alloys by an in-situ reaction. [dissertation]. Hohhot (China): Inner Mongolia University of Technology. 2020.

[40] Wang FC, Li JJ, Shi CS, Liu EZ, He CN, Zhao NQ. Orientation relationships and interface structure in $MgAl_2O_4$ and $MgAlB_4$ Co-Reinforced Al matrix composites. ACS Appl Mater Interfaces 2019;11(45):42790–800. https://doi.org/10.1021/acsami.9b14923.

[41] Wang S, Lin XB, Rong XD, Zhang X, Zhao DD, He CN, Zhao NQ. The role of Mg content in regulating microstructures and mechanical properties of Al-Mg-ZnO composites fabricated via in-situ reaction sintering. Compos B Eng 2024;281:111565. https://doi.org/10.1016/j.compositesb.2024.111565.

[42] Thakur A, Gupta RK, Udhayabanu V, Peshwe DR, Mahajan YY. Ultrasonic assisted reactive synthesis and characterization of Al-$MgAl_2O_4$ in-situ composite. Mater Chem Phys 2023;297:127311. https://doi.org/10.1016/j.matchemphys.2023.127311.

[43] Kim CS, Cho K, Manjili MH, Nezafati M. Mechanical performance of particulate-reinforced Al metal-matrix composites (MMCs) and Al metal-matrix nano-composites (MMNCs). J Mater Sci 2017;52:13319–49. https://doi.org/10.1007/s10853-017-1378-x.

[44] Khajuria A, Kumar R, Bedi R. Effect of boron addition on creep strain during impression creep of P91 steel. J Mater Eng Perform 2019;28:4128–42. https://doi.org/10.1007/s11665-019-04167-z.

[45] Singh A, Khajuria A, Bedi R, Dommeti SG, Shiva S. Microstructural and mechanical property analysis of high-strength low-alloy steel tubes fabricated using wire arc-directed energy deposition technique. Met Mater Int 2025;31:1815–35. https://doi.org/10.1007/s12540-024-01849-9.
[46] Akhtar M, Khajuria A, Kumar VS, Gupta RK, Shaju K, Albert SK. Evolution of microstructure during welding simulation of Boron modified P91. Steel Times 2019;120:672–85. https://doi.org/10.1134/s0031918x19070056.
[47] Khajuria A, Misra A, Shiva S. On the heat-affected Zone role for mechanical properties of structural-steel MIG and CMT–MIG weldments. Trans Indian Inst Met 2024;77:3905–13. https://doi.org/10.1007/s12666-024-03460-3.
[48] Yang R. Preparation of in-situ aluminum matrix composites and friction stir processing. [dissertation]. Zhenjiang Jiangsu Univer 2017:15–21.
[49] Liu PR, Hao SM, Wu HZ, Wang HF, Xie JP. Synergistic enhancement of strength and plasticity of SiCp/Al composites by designing and controlling SiCp@$MgAl_2O_4$ core-shell micro-interfaces. Ceram Int 2023;49:41016–21. https://doi.org/10.1016/j.ceramint.2023.10.034.
[50] Li XN, Liu ZY, Luo HJ, Ma K, Xiao BL, Wang D, Ma ZY. Enhancing strength-ductility synergy of graphene/Al-Cu-Mg composites via forming $MgAl_2O_4$@graphene complex structure. Compos Commun 2023;43:101737. https://doi.org/10.1016/j.coco.2023.101737.
[51] Zhang Z, Nie KB, Deng KK, Xu C. Preparation of low-cost, high-strength and fast-dissolving (MgO-Al_3Fe)/AZ91 magnesium matrix composites using a novel in-situ reaction. Compos Commun 2024;49:101986. https://doi.org/10.1016/j.coco.2024.101986.
[52] Chankitmunkong S, Eskin DG, Limmaneevichitr C. Structure refinement, mechanical properties and feasibility of deformation of hypereutectic Al–Fe–Zr and Al–Ni–Zr alloys subjected to ultrasonic melt processing. Mater Sci Eng, A 2020;788:139567. https://doi.org/10.1016/j.msea.2020.139567.
[53] Zhang Z, Chen D. Consideration of Orowan strengthening effect in particulatereinforced metal matrix nanocomposites: a model for predicting their yield strength. Scr Mater 2006;54:1321–6. https://doi.org/10.1016/j.scriptamat.2005.12.017.
[54] Liang YH, Shi ZM, Li GW, Zhang RY, Zhao G. Effects of Er addition on the crystallization characteristic and microstructure of Al–2wt%Fe cast alloy. J Alloys Compd 2019;781:235–44. https://doi.org/10.1016/j.jallcom.2018.12.063.
[55] Gao T, Hu JY, Li CX, Liu GL, Liu XF. In-situ fabrication of a strong and stiff $MgAl_2O_4$/Al-based composite. Compos Commun 2024;52:102115. https://doi.org/10.1016/j.coco.2024.102115.
[56] Pu BW, Lin XB, Li BW, Chen XF, He CN, Zhao NQ. Effect of SiC nanoparticles on the precipitation behavior and mechanical properties of 7075Al alloy. J Mater Sci 2020;55:6145–60. https://doi.org/10.1007/s10853-020-04381-4.
[57] Chen YY, Nie JF, Wang F, Yang HB, Wu CC, Liu XF, Zhao YH. Revealing hetero-deformation induced (HDI) stress strengthening effect in laminated Al-(TiB_2+TiC)p/6063 composites prepared by accumulative roll bonding. J Alloys Compd 2020;815:152285. https://doi.org/10.1016/j.jallcom.2019.152285.
[58] Sharma A, Morisada Y, Ushioda K, Fujii H. Elucidation of the factors controlling interface decohesion and particle fracture in a friction stir alloyed Al–Fe alloy system. Materialia 2024;34:102066. https://doi.org/10.1016/j.mtla.2024.102066.
[59] Zhang Q, Xiao BL, Wang WG, Ma ZY. Reactive mechanism and mechanical properties of in situ composites fabricated from an Al-TiO_2 system by friction stir processing. Acta Mater 2012;60:7090–103. https://doi.org/10.1016/j.actamat.2012.09.016.
[60] Fribourg G, Brechet Y, Deschamps A, Simar A. Microstructure-based modelling of isotropic and kinematic strain hardening in a precipitation-hardened aluminium alloy. Acta Mater 2011;59:3621–35. https://doi.org/10.1016/j.actamat.2011.02.035.
[61] Xu ZH, Zhang X, Zhao NQ, He CN. Synergistic strengthening effect of in-situ synthesized WC_{1-x} nanoparticles and graphene nanosheets in copper matrix composites. Compos Appl Sci Manuf 2020;133:105891. https://doi.org/10.1016/j.compositesa.2020.105891.